Impact of Indian Ocean Dipole on the mesoscale eddies and their energy in the Bay of Bengal

Navin Chandra [1,2], Vimlesh Pant [1,*]

Abstract

Oceanic mesoscale eddies and their physical and dynamical characteristics are studied using a high-resolution numerical model in the Bay of Bengal (BoB), a semi-enclosed bay based in the northeast Indian Ocean (IO). The formation, duration, and kinetic energy of these eddies are primarily influenced by the intensity of surface currents, upper-ocean stratification, and regional bathymetry. The Indian Ocean Dipole (IOD) is a dominant mode of interannual variability in the IO, which influences ocean currents in the BoB apart from the well-known dipole observed in sea surface temperature between eastern and western IO. The high-resolution numerical experiments with positive and negative phases of IOD atmospheric forcing reveal the influence of anomalous circulation prevailing in the negative IOD (nIOD) and positive IOD (pIOD) on mesoscale eddies and their kinetic energy in the BoB. A notable disparity in the eddies' characteristics was observed in both nIOD and pIOD and compared to normal years. In pIOD or nIOD, the number of eddies enhanced but their average lifespan reduced in the BoB. The increase in eddies was higher (38%) in nIOD than pIOD (11.2%) when compared to normal (non-IOD) years. The contribution of eddies to the total eddy kinetic energy (EKE) of the BoB increased from about 10% in normal years to about 25% in either of the IOD phases. The largest influence of IOD is seen at the thermocline depth. Within the BoB, the Andaman Sea region experienced the largest variations in eddies during IOD years.

Keywords

Mesoscale eddies; Indian Ocean Dipole; Bay of Bengal; Numerical Ocean model; Eddy kinetic energy

[1] Centre for Atmospheric Sciences, Indian Institute of Technology Delhi, New Delhi, India
[2] National Centre for Medium Range Weather Forecasting, Ministry of Earth Sciences, Noida, India
*Correspondence: vimlesh@cas.iitd.ac.in (V. Pant)

Abbreviations

AdS Andaman Sea

AE Anticyclonic Mesoscale Eddies

AS Arabian Sea

BoB Bay of Bengal

BOMA Bureau of Meteorology Australia

CBoB Central Bay of Bengal

CC Correlation Coefficient

CE Cyclonic Mesoscale Eddies

DJF December–January–February

DMI Dipole Moment Index

EICC East India Coastal Current

EKE Eddy Kinetic Energy

IO Indian Ocean

IOD Indian Ocean Dipole

JJA June–July–August

KPP K-Profile Parameterization

KW Kelvin Wave

MAM March–April–May

nBoB Northern Bay of Bengal

NIOA North Indian Ocean Atlas

nIOD Negative IOD

OGCM Ocean General Circulation Model

OW Okubo Weiss Parameter

PBIAS Percentage Bias

pIOD Positive IOD

RMSE Root Mean Square Error

ROMS Regional Ocean Modelling System

RW Rossby Wave

SBoB Southern Bay of Bengal

SKE Surface Kinetic Energy

SLA Sea Level Anomaly

SON September–October–November

SSS Sea Surface Salinity

SST Sea Surface Temperature

Symbols

g Acceleration due to gravity

KE_g Geostrophic Kinetic Energy

u_g Geostrophic Zonal Velocity

v_g Geostrophic Meridional Velocity

u Zonal Velocity

v Meridional Velocity

X Euclidean Distance

S_n Normal Component of Strain Tensor

S_s Shear Component of Strain Tensor

θ_b Bottom Stretching Parameter

θ_s Surface Stretching Parameter

ξ Vertical Componet of Relative Vorticity

η Sea Surface Height

1. Introduction

The BoB is a semi-enclosed basin situated in the northern sector of the IO. The northern region of the BoB receives a significant influx of freshwater during the monsoon and post-monsoon seasons. The discharge of water aids in the transportation of excess low-salinity water towards the tropical IO and Arabian Sea (AS) through the East India Coastal Current (EICC). Therefore, the presence of stratification due to freshwater influx from rivers has a significant role in shaping the dynamics of this specific geographic region (Hormann et al., 2019). The water circulation patterns within the BoB are influenced by the biannual shift in monsoon winds, resulting in consequential

impacts on the oceanic currents (Eigenheer and Quadfasel, 2000; Shankar et al., 2002; Shetye et al., 1993). Furthermore, the circulation patterns within the BoB are subject to various local and remote factors. The circulation patterns are influenced by local driving forces, such as wind stress, and remote forcing elements, such as coastal Kelvin Wave (KW) and Rossby Wave (RW) (Aparna et al., 2012; Shankar and Shetye, 1999). Numerous study attempts have been conducted to gain a comprehensive understanding of the complexities of the BoB and the diverse significant variables that contribute to its dynamics. These factors encompass the semi-annual reversal of monsoon winds, freshwater discharge, tidal energy, and remote forcing, such as coastal KW and RW. These investigations have employed observational and numerical methodologies (Jensen et al., 2016; Sadhukhan and Chakraborty, 2023; Sandeep and Pant, 2018; Yu et al., 1991).

One significant factor contributing to the alteration of remote forcing is the IOD, a phenomenon that manifests in the equatorial region of the IO. The identification of the IOD was first reported by Saji et al. (1999). The quantification of the strength of the phenomena can be achieved by using the ongoing evaluation of the dipole moment index (DMI). The DMI is ascertained through the computation of the disparities between the anomalies in sea surface temperature (SST) within two specific regions: one encompassing the area between 50°E–70°E, 10°S–10°N, and the other extending from 90°E–110°E, 0°–10°S. The IOD is a climatic phenomenon that manifests in the equatorial region of the IO. Nevertheless, the influence of this phenomenon extends beyond the equatorial areas and exerts substantial consequences on the northern IO through direct and indirect forcing mechanisms. Direct forcing encompasses factors such as wind, while indirect forcing involves the influence of coastal KW and RW (Aparna et al., 2012; Thompson et al., 2006).

The IOD exerts a substantial influence on the physical and dynamical characteristics of the BoB. Its impact goes beyond the equatorial areas and encompasses the subtropical regions, affecting various dynamical and physical phenomena (Anila and Gnanaseelan, 2023). There exists a positive correlation between the IOD events and the amount of rainfall during the Indian summer monsoon. The phenomenon of IOD is characterized by the unusual convergence and divergence of winds. The pIOD events are associated with increased precipitation, resulting in surplus rainfall in the BoB region. Conversely, nIOD events are linked to a decrease in precipitation, leading to a deficit in rainfall within the same BoB region, further changing the freshwater discharge through rivers (Ashok et al., 2004; Behera et al., 1999; Saji et al., 1999). The study reveals that during a pIOD event, the BoB exhibits a negative anomaly in SST, which is positively correlated with the DMI (Chanda et al., 2018). The role of pIOD on the upwelling feature in the southwest coast of India was examined by Nigam

et al. (2018), which says that during pIOD years, Ekman transport is reduced, which results in warmer SST. During a pIOD year, BoB exhibits a negative anomaly in SST. Remote forcings and local winds in the BoB are closely linked to IOD events and have a significant effect on how the BoB boundary currents change from year to year. During pIOD years, a coastal phenomenon known as coastal Kelvin Waves propagates along the entire periphery of the BoB, resulting in the disorganization and weakening of the EICC. This weakening is primarily attributed to the prevalence of mesoscale oceanic eddies. Conversely, during nIOD years, anomalous strong winds induce elevated sea level anomalies (SLA), leading to the intensification of the EICC and its associated gyres. The generation of mesoscale meanders and eddies occurs along the path of the EICC due to the instability of the background flow. Open-ocean eddies can influence the flow of the EICC due to their inclination to travel towards the west following their formation in the middle and eastern BoB (Dandapat et al., 2018; Sherin et al., 2018).

The prevalence of mesoscale oceanic eddies in the BoB region can be attributed to a mix of local and remote forcings, as well as internal oceanic instability. The existence of various local and remote factors during varied IOD situations inherently results in fluctuations in mesoscale oceanic eddies and their corresponding energy across different IOD scenarios. Numerous studies have been conducted to investigate the variability of SST, wind anomalies, SLA, surface currents, and other dynamic factors. These investigations have utilized a combination of observational data and modelling techniques, exploring various IOD scenarios. However, to date, no comprehensive research has been conducted to investigate the characteristics of mesoscale

oceanic eddies in relation to the different IOD circumstances. In the present study, we have endeavoured to address this gap in the existing research. Using a numerical model, we have conducted an investigation of the mesoscale oceanic eddies in the BoB, specifically focusing on cyclonic mesoscale oceanic eddies (CE) and anticyclonic mesoscale oceanic eddies (AE). In order to accurately depict the mesoscale oceanic structure, it is necessary for the Ocean General Circulation Model (OGCM) to possess a resolution of around 10 km or finer (Lin et al., 2019). The limited resolution of available observation or reanalysis data for resolving mesoscale oceanic eddies necessitates the utilization of a numerical model for conducting this investigation. The numerical model utilized in this study possesses a horizontal resolution that enables the resolution of mesoscale marine eddies, namely those within a spatial scale of 10–100 km. Therefore, throughout the remainder of this work, the terms 'eddies' or 'mesoscale eddies' should be considered synonymous.

2. Model, data, and methodology

2.1 Numerical model

In the present study, the Regional Ocean Modelling System (ROMS) was employed. ROMS is a publicly available computational model that was developed by Rutgers University, USA. The model employed is a hydrostatic, free surface model that utilizes a sigma coordinate system that follows the terrain (Song and Haidvogel, 1994). The ROMS model provides users with the capability to manipulate the distribution of the vertical grid in the water column by adjusting the surface and bottom stretching parameters (Haidvogel et al., 2008). ROMS uses the Arakawa C grid (Arakawa
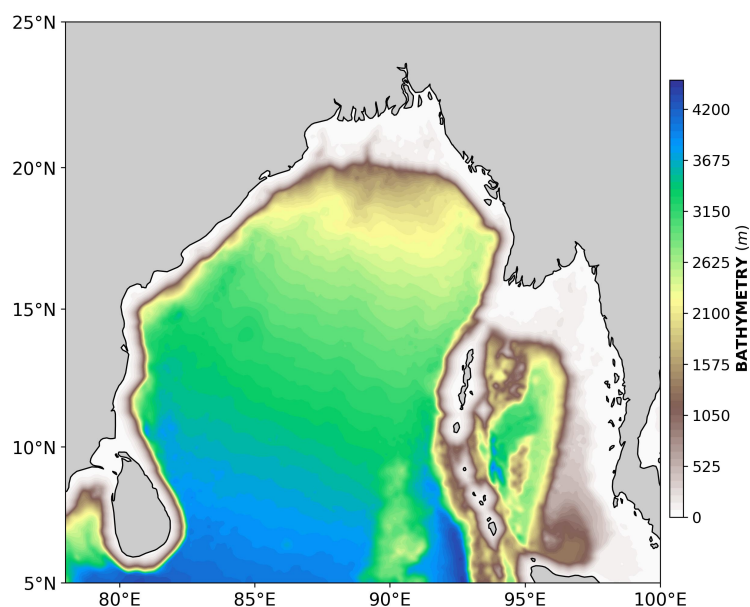

Figure 1. Model domain and bathymetry (m) derived using ETOPO2v2.

and Lamb, 1977) to solve the primitive equation system numerically, incorporating the Boussinesq approximation (Zeytounian, 1990). A comprehensive explanation of the physical and dynamical algorithms utilized in the ROMS is provided in great depth by (Haidvogel et al., 2008; Shchepetkin and McWilliams, 2005, 2003, 1998). The ROMS has strong performance in simulating basin-scale phenomena and has obtained significant adoption within the scientific community (Chassignet et al., 2000; Haidvogel et al., 2000; Marchesiello et al., 2003; Nigam et al., 2018; Sandeep and Pant, 2018; Song and Haidvogel, 1994).

Figure 1 shows the study domain (78°E–100°E, and 5°N–25°N) configured for ROMS and bathymetry (in meters) using a color scale. ETOPO2v2 data is used for bathymetry and interpolated on the horizontal resolution of $\frac{1}{18°}$ (5.95 km), making the model capable of capturing mesoscale eddies of space scale of 10–100 km. The model includes 50 sigma levels, each characterized by a surface stretching parameter (θ_s) and a bottom stretching parameter (θ_b), and a critical depth of 10 m. The eastern and northern sides of the lateral boundary are closed, while the southern and western sides are open. The Smagorinsky parameterization technique (Smagorinsky, 1963) was

employed for horizontal mixing, while the K profile parameterization (KPP) (Large et al., 1994) was utilized for vertical mixing. The open boundary condition employs a radiation and nudging strategy to handle the traces and velocities.

2.2 Experiment design

The years spanning from 1980 to 2018 have been classified into three distinct groups, namely pIOD years, nIOD years, and normal years, with the assistance from the Bureau of Meteorology Australia (BOMA) year-wise details in Table 1.

The ROMS model was cold started using initial and lateral boundary conditions from SODA3.3.2 (Carton et al., 2018), which is a 3d ocean reanalysis data having horizontal resolution of $\frac{1}{4°} \times \frac{1}{4°}$ and 50 vertical sigma levels. Daily atmospheric forcing for wind stress and air-sea fluxes were created using the Tropflux dataset, and surface freshwater flux was calculated using total precipitation and surface evaporation from ERA5 (Copernicus Climate Change Service, 2023). Monthly climatological freshwater discharge as a point source at the land-sea interface was supplied using "Dai and Trenberth Global River Flow and Continental Discharge" data (Dai, 2017).
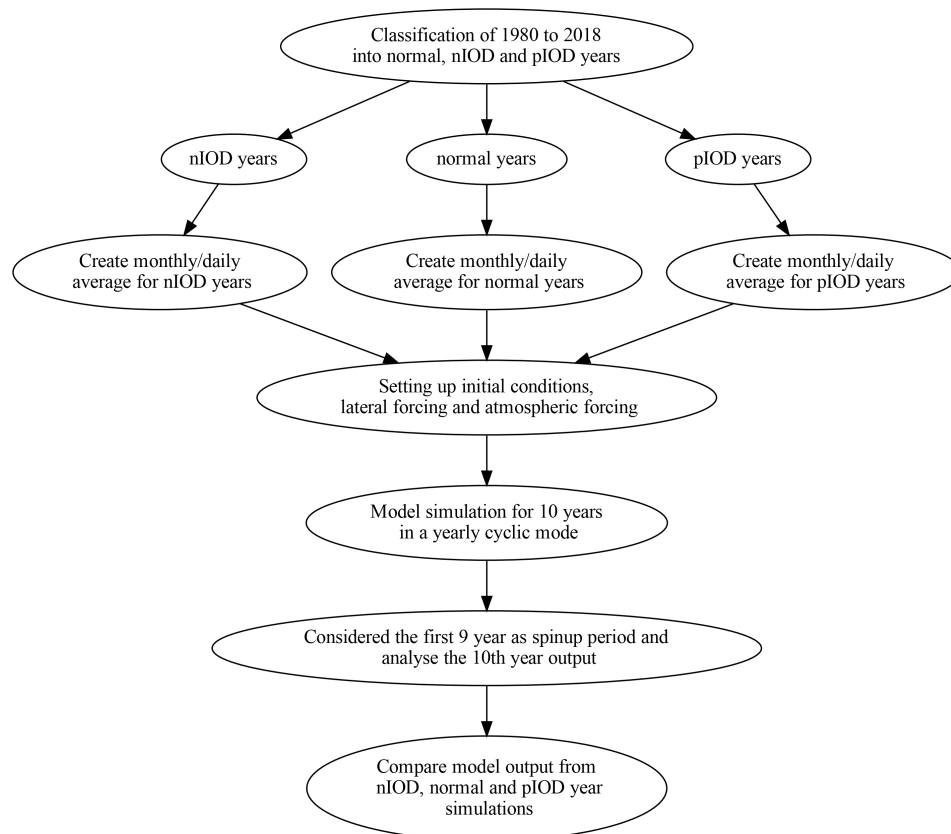

Figure 2. Flowchart of the numerical experiments designed to study the impact of IOD on eddies.

Table 1. List of normal years, positive IOD (pIOD) years and negative IOD (nIOD) years based on the Bureau of Meteorology Australia from 1980 to 2018.

IOD MODE	Years	Total Years
NORMAL	1980, 1984, 1985, 1986, 1987, 1988, 1990, 1991, 1993, 1995, 1999, 2000, 2001, 2002, 2003, 2004, 2005, 2007, 2008, 2009, 2011, 2013, 2017, 2018	24
pIOD	1982, 983, 1994, 1997, 2006, 2012, 2015	7
nIOD	1981, 1989, 1992, 1996, 1998, 2010, 2014, 2016	8

Figure 2 depicts the experimental design using a flow-chart. The data from 1980 to 2018 was first divided into three categories: normal years, pIOD years, and nIOD years. Subsequently, the preprocessing files, such as atmospheric forcing, initial forcing, and lateral forcing, were generated utilizing segregated data. The model was cold started to execute three simulations for normal years, nIOD years, and pIOD years, each spanning 10 years. The initial nine years of output were considered a spin-up period, whereas the output from the tenth year was utilized for analysis.

2.3 Eddy detection and tracking

There can be multiple methods to detect the eddies or vortex inside a fluid flow. Epps (2017) categorised the methods for vortex detection in the generalised field of fluid mechanics into four categories which are eulerian non-local vortex identification method, eulerian local region-type vortex identification, eulerian local line-type vortex identification and lagrangian vortex-identification methods. In the field of naval hydrodynamics, Zhao et al. (2020) had classified the vortex identification into three categories which are basically based on vorticity, velocity gradient, helicity and pressure criteria. In the field of physical oceanog-

raphy, Lian et al. (2019) have divided the eddy detection primarily in three categories based on: a) algorithms that rely on rotational flow, b) algorithms that rely on closed contours of SLA, and c) a hybrid method that combines both a) and b). The current study utilizes a hybrid technique (Halo, 2012; Halo et al., 2014) for detecting eddies. This approach combines both geometric and dynamic methods to detect eddies. The geometrical method (Chelton et al., 2011) detects closed contours of SSH, whereas the dynamical method (Chelton et al., 2007; Isern-Fontanet et al., 2006) detects regions with a negative Okubo-Weiss parameter (OW) (Okubo, 1970; Weiss, 1991) A negative OW value shows that the flow is dominated by the vorticity. The OW is defined as

$$OW = S_n{}^2 + S_s^2 - \xi^2 \tag{1}$$

$$S_n = \frac{\partial u}{\partial x} - \frac{\partial v}{\partial y} \tag{2}$$

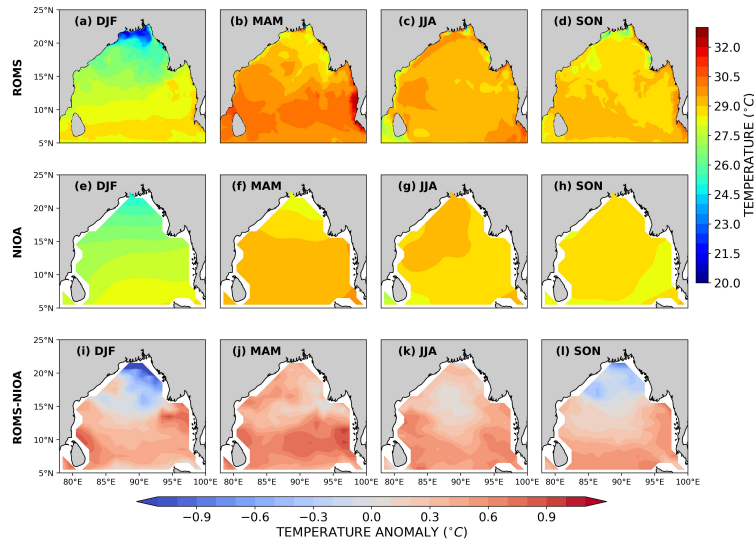$$S_s = \frac{\partial v}{\partial x} + \frac{\partial u}{\partial y} \tag{3}$$

Figure 3. Spatial comparison of simulated ROMS SST (°C) in the first row, and observed NIOA SST (°C) in the middle row and the difference (ROMS-NIOA) in the lower row. Subplots a, b, c, and d represent ROMS SST for DJF, MAM, JJA, and SON seasons respectively. Subplots e, f, g, and h represent NIOA seasonal SST and subplots i, j, k, l represent the seasonal bias (ROMS-NIOA).

$$\xi = \frac{\partial v}{\partial x} - \frac{\partial u}{\partial y} \tag{4}$$

$$u_g = \frac{-g\partial[\eta]}{f\partial y}, \quad v_g = \frac{g\partial[\eta]}{f\partial x} \tag{5}$$

The variables u_g and v_g represent the meridional and zonal components of the surface geostrophic current, g denotes the acceleration due to gravity, f represents the Coriolis parameter, and η represents the SSH, S_s is the shear component of the strain tensor, S_n is the normal component of the strain tensor and ξ is the vertical component of the relative vorticity. The computation of OW requires using second-order derivatives of SSH, which introduces significant amounts of noise. The geometrical technique is not affected by this noise problem, although it does have several adjustable parameters that are associated with SSH. By integrating the OW and geometrical technique, the algorithm's sensitivity to adjustable parameters decreases, resulting in more reliable and resilient outcomes.

The major benefit of using a hybrid approach is the removal of meanders detected as eddy. In the hybrid approach, first OW is calculated, and regions with $OW < 0$ are identified as the regions dominated by the vorticity. Next, the geometrical method is applied and closed contours are detected. If regions with negative OW are within a close contour of SSH, only then it is identified as an eddy.

After the detection of eddies over a defined timesteps, eddies were tracked with the help of nondimensional space property called as Euclidean distance (X) (Penven et al., 2005) defined as:

$$X_{(e1,e2)} = \sqrt{\left(\frac{\Delta X}{X_0}\right)^2 + \left(\frac{\Delta R}{R_0}\right)^2 + \left(\frac{\Delta\xi}{\xi_0}\right)^2} \tag{6}$$

ΔX is the distance between eddy centres at time t_1 and t_2, ΔR is the diameter variation and $\Delta\xi$ is the change in the vorticity. Values of X_0, R_0 and ξ_0 is 25 km, 200 km and $10^{-5}\ S^{-1}$ respectively. If the vorticity changes from positive to negative or vice-versa $X_{(e1,e2)}$ considered as infinite to preserve the eddy polarity. A threshold value of 0.3 m s^{-1} (Varna et al., 2023) is considered for the eddy translational speed. In case any eddy having speed more than the threshold value, it is considered unrealistic drift and treated as a different eddy.

3. Results

3.1 Model validation

The ROMS model was set up for the BoB region as depicted in Figure 1. The simulated findings of SST and sea surface salinity (SSS) in ROMS were validated against the North Indian Ocean Atlas (NIOA) (Chatterjee et al., 2012) on a seasonal basis. NIOA data is based on the World Ocean Atlas with additional data included from the Indian sources to improve it specifically in the Indian Exclusive Economic Zone for annual, seasonal, and monthly climatology. The NIOA data has a horizontal resolution of 1°. Figures 3 and 4 show the validation results for SST and SSS, respectively. The model effectively replicates the fluctuations in SST on a seasonal basis. The geographical bias remains within the range of $\pm 1.2°$. Except for the post-monsoon and
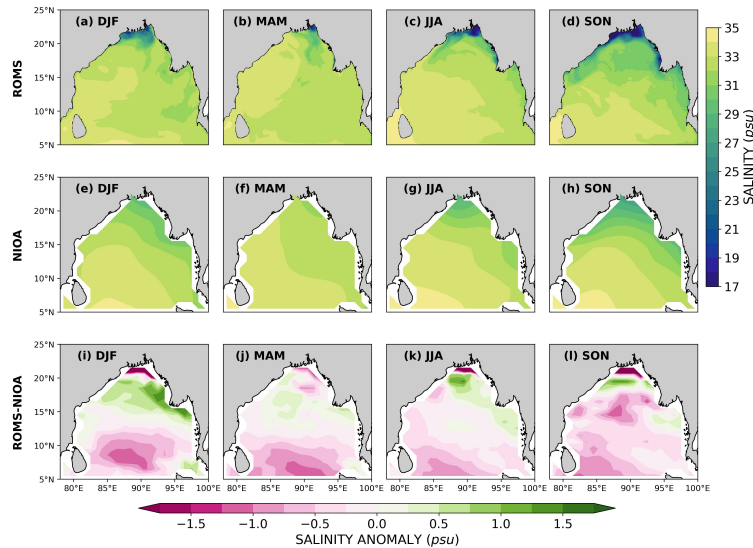

Figure 4. Comparison of simulated ROMS SSS (psu) in the first row, and observed NIOA SSS (psu) in the middle row and the difference (ROMS-NIOA) in the lower row. Subplots a, b, c, and d represent ROMS SSS for DJF, MAM, JJA, and SON sea-sons respectively. Subplots e, f, g, h represent NIOA seasonal SSS and subplots i, j, k, l represent the seasonal bias (ROMS-NIOA).
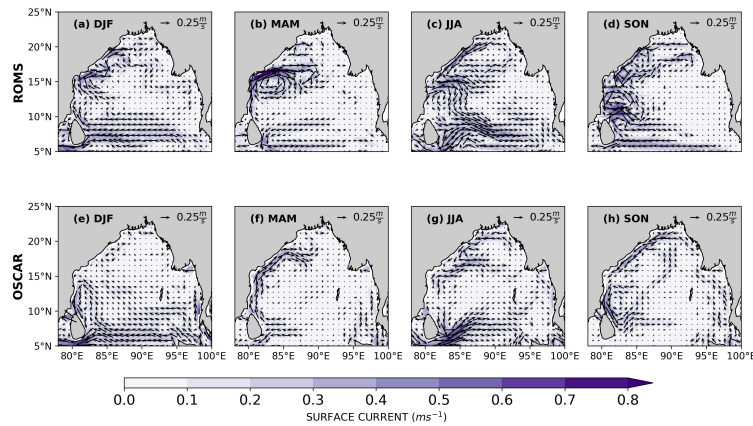
Figure 5. Comparison of simulated surface currents (ROMS) with observed surface currents (OSCAR) on a seasonal basis. Subplots a, b, c, and d represent the DJF, MAM, JJA and SON seasons from ROMS output whereas subplots e, f, g, h represents observed (OSCAR) seasonal surface currents for DJF, MAM, JJA, SON seasons respectively.
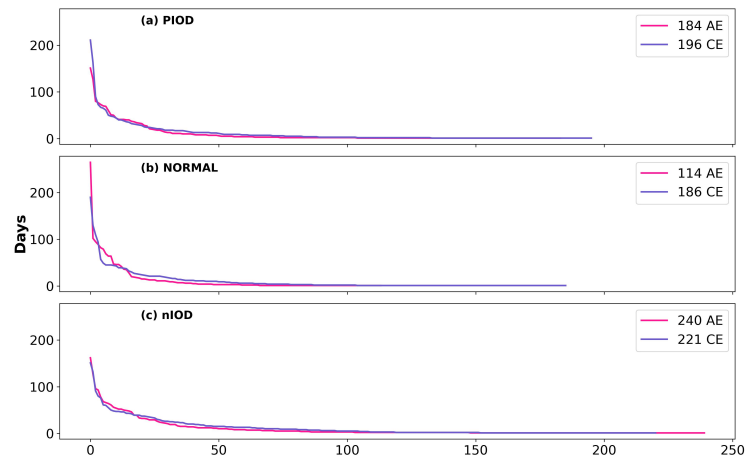

Figure 6. The x-axis in the plot represents the uniquely detected Anticyclonic Eddies (AE) and Cyclonic Eddies (CE) in the decreasing order of their lifespan. The y-axis represents the life of the eddy. Subplots a, b, and c represent the eddy lifespan in decreasing order for negative IOD (nIOD) years, normal years, and positive IOD (pIOD) years respectively.

winter seasons, the model exhibits a positive bias. However, during these periods, the model shows a negative bias in the head bay region. The model accurately captures the seasonal fluctuations and patterns of SST. Further, the model adequately captures the subsurface temperature when compared with moored buoys (supplementary Figure S1).

The model adequately represents the fluctuations in SSS, taking into account the additional influx of freshwater. The bias in SSS ranges from ± 1.5 psu. Throughout the entire season, SSS exhibits a negative bias in the southern Bay of Bengal (BoB) and a mixed bias in the northern BoB. The bias typically remains below ± 1 psu in most regions, with greater values observed exclusively in isolated coastal areas. The root mean square error (RMSE) and correlation coefficient (CC) values for SST are 0.65 and 0.78 respectively, while for SSS they are 0.86 and 0.88. These values are obtained by comparing the yearly aver-

aged model data with NIOA data. A comparison of model-simulated salinity profiles with moored buoy observations shows a good agreement between the model and observations at different locations in the BoB (supplementary Figure S2).

Figure 5 depicts the seasonal comparison between the surface currents simulated by ROMS and the measured currents (OSCAR). The model effectively reflects the periodic variations in both the orientation and intensity of surface currents. The EICC moves in a southerly direction during the early northeast (winter) monsoon and then changes its course to move northward, reaching its peak intensity in April–May during the southwest (summer) monsoon. The EICC undergoes development in November, experiences a decrease in strength in December, and eventually dissipates in January. In January, the monsoon current moves in a westward direction to the south of Sri Lanka. However, in May–June, it changes its direction and travels eastward.

Table 2. The number of uniquely detected Anticyclonic Eddies (AE), Cyclonic Eddies (CE), total eddies (AE+CE) and the average life in days for the negative IOD (nIOD) years, normal years, and positive IOD (pIOD) years.

	No of Eddies				Average Life of Eddies (days)		
	AE	CE	Total		AE	CE	Total
NORMAL	114	186	300		14.6	10.4	12.03
pIOD	184	196	380		9.93	11.1	10.53
nIOD	240	221	461		9.8	11.9	10.8

3.2 Impact of IOD

Table 2 shows the number of detected eddies and the average lifespan of the eddies during a normal year, nIOD year and pIOD year. Figure 6 depicts the same in a line graph where uniquely detected eddies are sorted in decreasing order of their life span and plotted against it for nIOD, normal and pIOD years. Table 3 gives the total eddy day (Total eddy day = Avg life of eddy × No. of eddies) for the AE, CE and combinedly for the AE and CE during a pIOD, normal and nIOD years.

From Tables 2 and 3 and Figure 6 we can clearly say that the eddy activity is increasing during an IOD year relative to a normal year. The eddy activity is even higher for a nIOD year. During an IOD year, the number of eddies increases but their life span are decreasing, where as in a normal years number of eddies are less but the life span of the eddy formed is longer. This clearly explains the increased eddy activity during an IOD year which is a result of the different remote forcing and local wind activity during different IOD conditions.

Daily comparisons for detected eddy numbers, the area covered by the eddies and the energy possessed by the detected eddies are shown in Figure 7a–c. Energy in plot 7(c) is the geostrophic kinetic energy (KE_g) (Chen et al., 2015; Wunsch, 2020).

Table 3. The total number of eddy days for Anticyclonic Eddy (AE), Cyclonic Eddy (CE), and total (AE+CE) for the negative IOD (nIOD) years, normal years, and positive IOD (pIOD) years.

	nIOD	NORMAL	pIOD
AE Eddy Day	2352	1664	1827
CE Eddy Day	2630	1934	2175
(AE+CE) Day	4978	3609	4014

$$KE_g = \frac{u_g^2 + v_g^2}{2} \tag{7}$$

(u_g and v_g calculated from equation 5).

Eddy counts for nIOD and pIOD year are always higher relative to normal year except for March and November–December months where eddy count is least for the pIOD year. During nIOD year the counts are always higher for the entire year. The area covered by the eddy shows similar variations like eddy count and has higher values for pIOD and nIOD year relative to normal year. For eddy energy too we have similar conditions except for the early part of the year, where the eddy energy of a normal year overlaps with the nIOD year and pIOD have the lowest energy and after a period when IOD arrives achieves its peak and weakens i.e. from June to September, the difference increase and
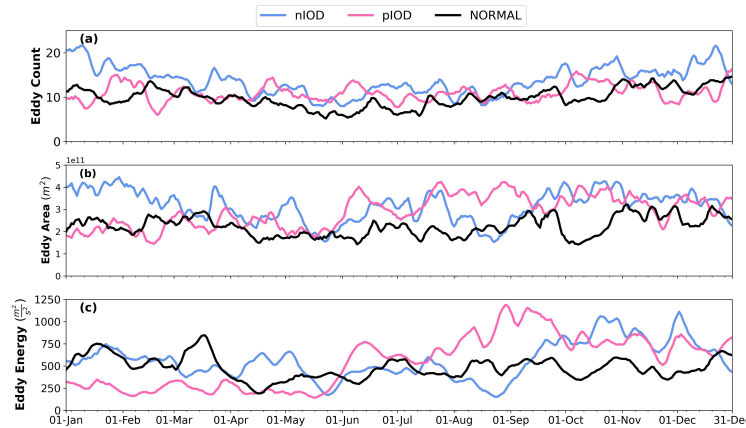
Figure 7. Comparison of daily detected eddy numbers, total covered surface area (m^2) and total kinetic energy (m^2 s^{-2}) possessed by them in subplots a, b and c respectively. The blue colour is for negative IOD (nIOD) years, pink for positive IOD (pIOD) years and black for normal years. The lines are smoothed by 5-day running mean data.
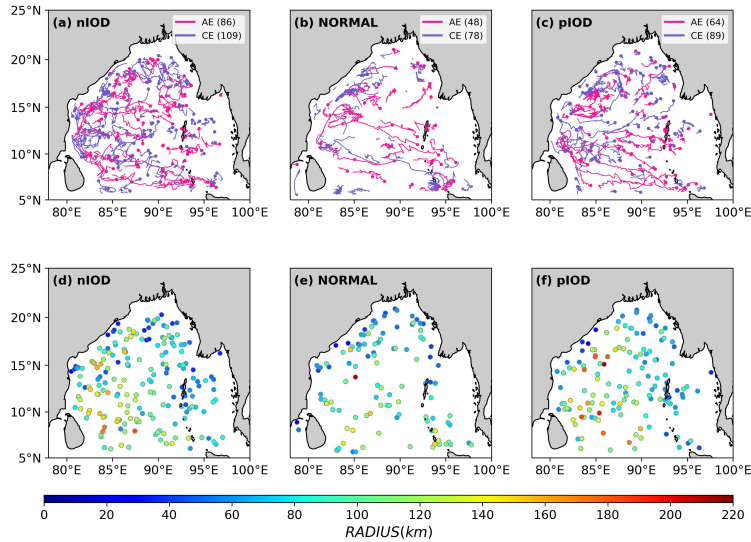
Figure 8. Subplots a, b, and c show the tracks for the negative IOD (nIOD) year, Normal year, and positive IOD (pIOD) year, respectively of the eddies in pink colour for Anticyclonic Eddy (AE), and blue colour for the Cyclonic Eddy (CE) having lifespan of at least 5 days. Dots show the eddy generation point and trails are the paths travelled by the eddies during their entire lifespan. Subplots d, e and f show the maximum radius attained by eddies during their entire lifespan for the corresponding eddies shown in subplots a, b, and c respectively. The magnitudes of the eddies' radius are given by the colour bar in km, the bubble size is uniform for all eddies.

normal year have the least value, nIOD and pIOD have the higher values.

Figure 8 clearly shows the spatial distribution of the eddies in the BoB for different IOD conditions. The eddy formation has increased in the entire BoB during both the negative and positive phase of IOD relative to a normal year, but the eddies formed during IOD condition are smaller in size and have a lower lifespan relative to a normal year. Eddies can be considered as the indirect way of measuring the turbulency of any spatial region. So, during an IOD phase, it is clear that the BoB saw the increased activity of the eddy not only in numbers but also in eddy-associated

energy during in IOD phase. This eddy-induced turbulency further increases when the IOD is in a negative phase.

The surface kinetic energy (SKE) of eddies is calculated using the following equation

$$SKE\,(\%) = \frac{KE_g \text{ of eddies}}{KE_g \text{ of BoB}} \times 100 \qquad (8)$$

Figure 9 shows the contribution of eddies in the SKE of BoB on a daily basis after smoothing with the 5-day running mean. In the early years the contribution by eddies overlaps for the nIOD, pIOD and normal years. Once the
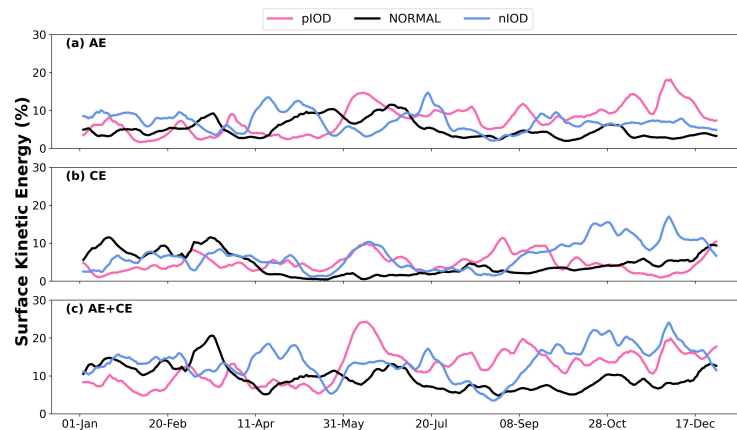

Figure 9. The contribution of eddies in the surface kinetic energy of BoB in percentage for Anticyclonic Eddy (AE) in subplot a, for the Cyclonic Eddy (CE) in subplot b and total (AE+CE) in subplot c. The red colour is for the positive IOD (pIOD) year, the blue colour for the negative IOD (nIOD) year and the black is for the normal year.

onset of IOD happens the contribution by the eddies in SKE increases. During IOD years EICC is mostly affected when it is equatorward i.e. in the boreal autumn (Dandapat et al., 2018). In Figure 9 we get the SKE value higher for the nIOD and pIOD during boreal autumn for both AE and CE. During the latter half part of the nIOD and pIOD years, contributions by eddies in SKE have increased. The mean percentage contribution of eddies in SKE is 12.47%, 9.5%, and 13.71% for the pIOD, nIOD, and normal year, respectively. The maximum contribution is 25.06%, 21.99%, and 25.6% for the pIOD year, normal year, and nIOD year, respectively. There is an increase of 3.61% during nIOD year and 3.07% during pIOD year relative to the normal year in maximum SKE by eddies, for the mean this change is 4.12% and 2.88%. This data suggests that the baroclinic instability increases more during a nIOD years, which is a major cause of eddy formation. Further, at the different oceanic depths, we have checked the eddy kinetic energy (EKE) (Chen et al., 2018) defined as:

$$\text{EKE} = \frac{1}{2}(u'^2 + v'^2) \qquad (9)$$

where u' and v' calculated from the 90-day running mean of meridional velocity (u) and zonal velocity (v) as 80% of eddies complete their lifecycle within this period (Chen and Han, 2019; Ji et al., 2020). Figure 10 displays the EKE

at various depths. It reveals that there is minimal variation in EKE at the surface during nIOD, pIOD, and normal years. However, as we descend from the surface, the disparity between pIOD and nIOD with the EKE of a typical year becomes increasingly apparent, and this discrepancy continues to grow with depth. In order to illustrate the disparity in EKE between nIOD, pIOD, and normal years at various depths, we have adjusted the y-axis scale differently for subplots 10a, 10b, 10c, 10d, and 10e. This was done to ensure that the contrasting magnitudes are clearly visible, as the magnitudes vary significantly at different levels, making it challenging to represent them on the same y-axis scale.

For a better comparison of EKE for nIOD and pIOD year relative to a normal year, we have calculated percentage bias (PBIAS) (Guo et al., 2022) defined as:

$$PBIAS = \left(\frac{\sum_{i=1}^{n} x_{+ve/-ve} - \sum_{i=1}^{n} x_{ref}}{\sum_{i=1}^{n} x_{ref}} \right) \times 100\% \quad (10)$$

The EKE of nIOD and pIOD is shown in equation 10 by x, and the EKE of a normal year is represented by the x_{ref}. We have calculated the PBIAS of EKE for nIOD and pIOD year relative to a normal year at different depth for the entire BoB and for the four different regions of BoB divided by geographical and climatical features in Figure 11. The region in Figure 11 with blue lines is the northern BoB
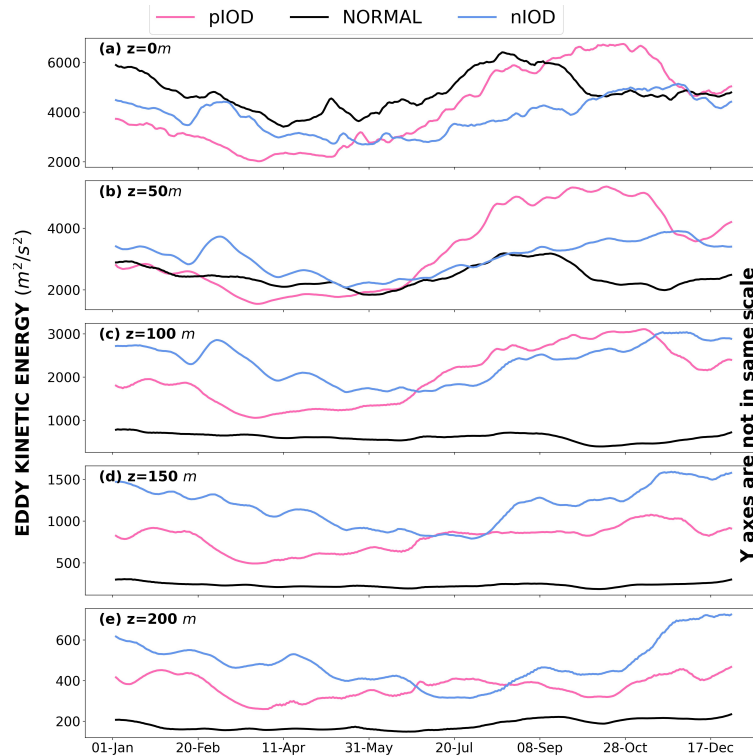

Figure 10. Eddy Kinetic Energy (EKE) at different oceanic depths. Subplots a, b, c, d, e represent the EKE at the surface, 50 m, 100 m, 150 m, and at the 200 m depth respectively. The pink line is for the positive IOD (pIOD) year, black for the normal year and blue for the negative IOD (nIOD) year.
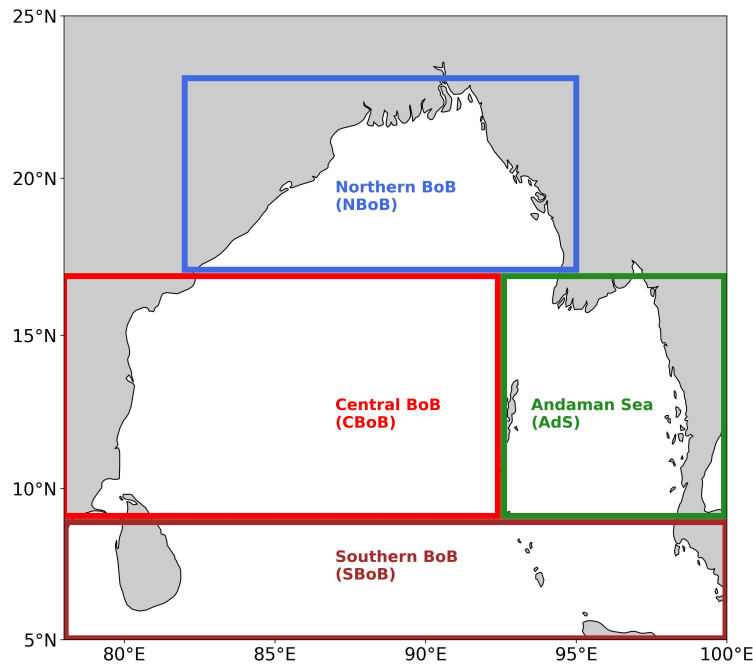
Figure 11. Four different regions of the Bay of Bengal (BoB), shown by different coloured boxes.

(nBoB) which receives a significant amount of freshwater discharge from rivers during monsoon and post-monsoon periods. The region surrounded by the green lines is the Andaman Sea (AdS) region, it is kind of cut off from the other parts of BoB due to the bathymetrical structure and the exchange of physical properties is limited. The southern part of the BoB (SBoB) is represented by the brown line and comes under the direct influence of the Indian Monsoon Current (IMC). The region in the red-coloured box is the central part of the BoB (CBoB) which covers most of the part influenced by the EICC, it also has the open ocean part of the BoB.

A comparison of PBIAS calculated from the model and ORAS5 data shows a good agreement in the surface and subsurface PBIAS in nIOD and pIOD years with respect to normal years. A larger difference in kinetic energy in nIOD than pIOD was observed in the thermocline depth in both model and ORAS5 data (shown in supplementary Figure S3). A higher resolution of the model than ORAS5 facilitates the identification of finer (up to 8 km radius) eddies in the model leading to higher kinetic energy (supplementary Figure S4) and a corresponding larger difference in PBIAS between nIOD and pIOD at the thermocline depth. The data shown in Figure 12 indicates that the maximum PBIAS value is not observed near the surface, but rather in the subsurface region between depths of 100 m to 200 m, which typically corresponds to the thermocline depth. This indicates that the influence of eddies was found to be largest at the thermocline region in the vertical column. Our results agree with the findings of Chaigneau et al. (2011). They used Argo profiles in the South Pacific

Ocean and reported that the greatest deviation in physical parameters such as temperature, salinity, and velocity of ocean water, induced by the existence of eddies, occurs exclusively at thermocline depth. The enhancement in the buoyancy frequency during the IOD years increases turbulence and internal wave activities in the thermocline zone (Yadidya and Rao, 2022). During IOD years KW is highly affected which further affects the circulation of the BoB. Normally two KW, sets of upwelling and downwelling forms during a year, first in January–March and second in August–September. During a pIOD year downwelling during the second KW is completely remains absent and only dominated by the upwelling because of the negative SSH. For pIOD year due to high SSH downwelling during the second KW becomes stronger (Aparna et al., 2012; Dandapat et al., 2018; Rao et al., 2010).

During the nIOD year value of PBIAS is maximum for AdS region relative to other regions of BoB except SON period. In nIOD year the subsurface stratification increases in the AdS which further enhances the activity of internal wave activity (Yadidya and Rao, 2022). During a pIOD year, the EICC experiences significant disruption and disorder due to the presence of mesoscale eddies. In contrast, during a nIOD year, the EICC remains organised and highly intensified. Additionally, the increase in RW activity, which propagates through the cBoB, generates mesoscale activities. The contribution of baroclinic activity to the high values of PBIAS is also significant. The reflected RWs propagating through the BoB create significant baroclinic activity in the AdS region. This is mostly owing to the intricate bathymetry and the existence of many seamounts in the
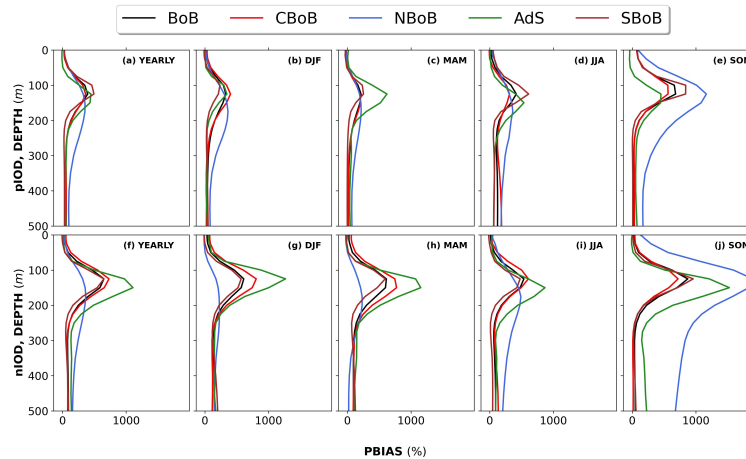
Figure 12. PBIAS of the Eddy Kinetic Energy (EKE) for the positive IOD (pIOD) and the negative IOD (nIOD) year relative to the normal year varying along the depth in y-axis. The subplots a, b, c, d and e is the Percentage Bias (PBIAS) for the pIOD year computed for the entire year, DJF, MAM, JJA and SON seasons respectively. The subplots f, g, h, i and j show the PBIAS of nIOD year for the entire year, DJF, MAM, JJA and SON seasons. The black color is for the complete Bay of Bengal (BoB), red is for the Central Bay of Bengal (CBoB), blue is for the Northern Bay of Bengal (NBoB), green is for the Andaman Sea region (AdS) and brown is for the Southern Bay of Bengal (SBoB) regions shown in Figure 11.

area. Consequently, during nIOD years, the baroclinic activity in the AdS region is particularly high, resulting in a high value of the PBIAS. As a result, the PBIAS found to increase by three orders of magnitude in thermocline depth in the AdS.

During the IOD years, the river catchment area in the northern and eastern parts of India experiences more precipitation. During a pIOD year, there is a significant increase in rainfall due to the intensified movement of moisture through the north-south monsoon circulation. However, during a nIOD year, there is an abnormal upward movement of air over the South China Sea, which leads to a decrease in rainfall over the eastern BoB. This results in a concentrated increase in rainfall in the river catchment area. Additionally, the KW are particularly strong during nIOD years (Behera and Ratnam, 2018). During a pIOD event, there is an increase in the surplus river discharge in the post-monsoon period (SON) in the Northern Bay of Bengal (NBoB). This increase in river discharge leads to enhanced baroclinic instability, which in turn causes an increase in the value of the PBIAS. During a nIOD year, there is an increase in rainfall specifically in the river catchment area and the significant activity of the KW, which collectively contribute to an increase in the value of PBIAS.

4. Conclusions

The BoB circulation is significantly impacted by both, local and remote driving factors. The two modes of the IOD exhibit distinct effects on the circulation of the BoB, both locally and through influences originating from afar. Multiple studies investigated the influence of the IOD on the circulation characteristics, SSH variations, and mixed layers in the BoB. However, the research gap in understanding the energy associated with different phases of IOD in the BoB motivated the current study. The model employed in this study effectively approximated the dynamic characteristics with high accuracy, as noticed in model validation. In this work, we investigated the alterations in the eddies and their evolving impact on the kinetic energy of the BoB. The outcome of the work yielded favourable results that were consistent with previous studies.

During an IOD year, there is an overall increase in eddy activity in the BoB compared to non-IOD years. The average lifespan of the eddy has dropped, but the number of eddies increased during an IOD year. This enhanced eddy activity in a more turbulent upper ocean during IOD years than normal years in the BoB. There is an increase of 11.2% in the total number of eddy days during pIOD years. Whereas during nIOD years, the increase is 38% compared to normal years. It has been observed that the intensity of eddy activities has intensified during the IOD phases. However, during the IOD, the size of eddies was decreased and their lifespan was shorter compared to normal years.

The impact of eddies on the EKE is more pronounced during IOD years as compared to normal years. In a normal year, the average value of EKE is 9.59% which enhances to 25.6% in nIOD, and 25% in pIOD years. This indicates a heightened level of eddy activity during IOD years. The eddies are known to influence subsurface properties in the water column. Figures 10 and 12 display the EKE and PBIAS of EKE at various depths. These figures reveal that the greatest disparity in EKE values occurs in the subsurface region at the thermocline depth, which magnifies during the IOD years. The PBIAS value in the NBoB increases to three orders of magnitude during nIOD event.

The Andaman Sea (AdS) region experiences the greatest impact during nIOD years, whereas the IMC region exhibits the highest PBIAS value during pIOD years. Seasonal variations significantly impact the EKE in different ways in the BoB. In years characterised by a nIOD, the AdS experiences the greatest influence on EKE. During the December-February period, the CBoB exhibits the highest PBIAS when the EICC flows towards the equator. Conversely, the AdS demonstrates the highest PBIAS during the MAM season, while the SBoB exhibits the highest PBIAS during the JJA period. During the pIOD years, the NBoB experiences the largest PBIAS due to an increase in freshwater discharge in north BoB during a positive phase of IOD.

Acknowledgements

Authors' contribution

NC and VP formed the draft's framework. The numerical simulations, analysis, and data visualization were performed by NC. The initial draft of the manuscript was prepared by NC, and VP made numerous corrections to improve its quality.

Supplementary materials

Please follow this link to see the supplementary material associated with this article.

References

Anila, S., Gnanaseelan, C., 2023. *Coupled feedback between the tropics and subtropics of the Indian Ocean with emphasis on the coupled interaction between IOD and SIOD*. Glob. Planet. Change 223, 104091.
https://doi.org/10.1016/j.gloplacha.2023.104091

Aparna, S.G., McCreary, J.P., Shankar, D., Vinayachandran, P.N., 2012. *Signatures of Indian Ocean Dipole and El Niño–Southern Oscillation events in sea level variations in the Bay of Bengal*. J. Geophys. Res. Oceans 117, 2012JC008055.
https://doi.org/10.1029/2012JC008055

Arakawa, A., Lamb, V.R., 1977. *Computational Design of the Basic Dynamical Processes of the UCLA General Circulation Model*, [in:] *Methods in Computational Physics: Advances in Research and Applications.* Elsevier, 173–265.
https://doi.org/10.1016/B978-0-12-460817-7.50009-4

Ashok, K., Guan, Z., Saji, N.H., Yamagata, T., 2004. *Individual and Combined Influences of ENSO and the Indian Ocean Dipole on the Indian Summer Monsoon*. J. Clim. 17, 3141–3155.
https://doi.org/10.1175/1520-0442(2004)017<3141:IACIOE>2.0.CO;2

Behera, S.K., Krishnan, R., Yamagata, T., 1999. *Unusual ocean–atmosphere conditions in the tropical Indian Ocean during 1994*. Geophys. Res. Lett. 26, 3001–3004.
https://doi.org/10.1029/1999GL010434

Behera, S.K., Ratnam, J.V., 2018. *Quasi-asymmetric response of the Indian summer monsoon rainfall to opposite phases of the IOD*. Sci. Rep. 8, 123.
https://doi.org/10.1038/s41598-017-18396-6

Carton, J.A., Chepurin, G.A., Chen, L., 2018. *SODA3: A New Ocean Climate Reanalysis*. J. Clim. 31, 6967–6983.
https://doi.org/10.1175/JCLI-D-18-0149.1

Chaigneau, A., Le Texier, M., Eldin, G., Grados, C., Pizarro, O., 2011. *Vertical structure of mesoscale eddies in the eastern South Pacific Ocean: A composite analysis from altimetry and Argo profiling floats*. J. Geophys. Res. Oceans 116, 2011JC007134.
https://doi.org/10.1029/2011JC007134

Chanda, A., Das, S., Mukhopadhyay, A., Ghosh, A., Akhand, A., Ghosh, P., Ghosh, T., Mitra, D., Hazra, S., 2018. *Sea surface temperature and rainfall anomaly over the Bay of Bengal during the El Niño-Southern Oscillation and the extreme Indian Ocean Dipole events between 2002 and 2016*. Remote Sens. Appl. Soc. Environ. 12, 10–22.
https://doi.org/10.1016/j.rsase.2018.08.001

Chassignet, E.P., Arango, H., Dietrich, D., Ezer, T., Ghil, M., Haidvogel, D.B., Ma, C.-C., Mehra, A., Paiva, A.M., Sirkes, Z., 2000. *DAMÉE-NAB: the base experiments*. Dynam. Atmos. Oceans 32, 155–183.
https://doi.org/10.1016/S0377-0265(00)00046-4

Chatterjee, A., Shankar, D., Shenoi, S.S.C., Reddy, G.V., Michael, G.S., Ravichandran, M., Gopalkrishna, V.V., Rama Rao, E.P., Udaya Bhaskar, T.V.S., Sanjeevan, V.N., 2012. *A new atlas of temperature and salinity for the North Indian Ocean*. J. Earth Syst. Sci. 121, 559–593.
https://doi.org/10.1007/s12040-012-0191-9

Chelton, D.B., Schlax, M.G., Samelson, R.M., 2011. *Global observations of nonlinear mesoscale eddies*. Prog. Oceanogr. 91, 167–216.
https://doi.org/10.1016/j.pocean.2011.01.002

Chelton, D.B., Schlax, M.G., Samelson, R.M., De Szoeke, R.A., 2007. *Global observations of large oceanic eddies*. Geo-

phys. Res. Lett. 34, 2007GL030812.
https://doi.org/10.1029/2007GL030812

Chen, G., Han, G., 2019. *Contrasting Short? Lived With Long? Lived Mesoscale Eddies in the Global Ocean*. J. Geophys. Res. Oceans 124, 3149–3167.
https://doi.org/10.1029/2019JC014983

Chen, G., Li, Y., Xie, Q., Wang, D., 2018. *Origins of Eddy Kinetic Energy in the Bay of Bengal*. J. Geophys. Res. Oceans 123, 2097–2115.
https://doi.org/10.1002/2017JC013455

Chen, X., Qiu, B., Chen, S., Qi, Y., Du, Y., 2015. *Seasonal eddy kinetic energy modulations along the North Equatorial Countercurrent in the western Pacific*. J. Geophys. Res. Oceans 120, 6351–6362. https://doi.org/10.1002/2015JC011054

Copernicus Climate Change Service, 2023. *Complete ERA5 global atmospheric reanalyis*.
https://doi.org/10.24381/CDS.143582CF

Dai, A., 2017. *Dai and Trenberth Global River Flow and Continental Discharge Dataset*.
https://doi.org/10.5065/D6V69H1T

Dandapat, S., Chakraborty, A., Kuttippurath, J., 2018. *Interannual variability and characteristics of the East India Coastal Current associated with Indian Ocean Dipole events using a high resolution regional ocean model*. Ocean Dynam. 68, 1321–1334.
https://doi.org/10.1007/s10236-018-1201-5

Eigenheer, A., Quadfasel, D., 2000. *Seasonal variability of the Bay of Bengal circulation inferred from TOPEX/Poseidon altimetry*. J. Geophys. Res. Oceans 105, 3243–3252.
https://doi.org/10.1029/1999JC900291

Epps, B., 2017. *Review of Vortex Identification Methods*. 55th AIAA Aerospace Sciences Meeting.
https://doi.org/10.2514/6.2017-0989

Guo, H., Zhan, C., Ning, L., Li, Z., Hu, S., 2022. *Evaluation and comparison of CMIP6 and CMIP5 model performance in simulating the runoff*. Theor. Appl. Climatol. 149, 1451–1470.
https://doi.org/10.1007/s00704-022-04118-0

Haidvogel, D.B., Arango, H., Budgell, W.P., Cornuelle, B.D., Curchitser, E., Di Lorenzo, E., Fennel, K., Geyer, W.R., Hermann, A.J., Lanerolle, L., Levin, J., McWilliams, J.C., Miller, A.J., Moore, A.M., Powell, T.M., Shchepetkin, A.F., Sherwood, C.R., Signell, R.P., Warner, J.C., Wilkin, J., 2008. *Ocean forecasting in terrain-following coordinates: Formulation and skill assessment of the Regional Ocean Modeling System*. J. Comput. Phys. 227, 3595–3624.
https://doi.org/10.1016/j.jcp.2007.06.016

Haidvogel, D.B., Arango, H.G., Hedstrom, K., Beckmann, A., Malanotte-Rizzoli, P., Shchepetkin, A.F., 2000. *Model evaluation experiments in the North Atlantic Basin: simulations in nonlinear terrain-following coordinates*. Dynam. Atmos. Oceans 32, 239–281.

https://doi.org/10.1016/S0377-0265(00)00049-X

Halo, I., 2012. *The Mozambique Channel eddies: Characteristics and mechanisms of formation*. Univ. Cape Town.

Halo, I., Backeberg, B., Penven, P., Ansorge, I., Reason, C., Ullgren, J.E., 2014. *Eddy properties in the Mozambique Channel: A comparison between observations and two numerical ocean circulation models*. Deep Sea Res. Pt. II 100, 38–53.
https://doi.org/10.1016/j.dsr2.2013.10.015

Hormann, V., Centurioni, L.R., Gordon, A.L., 2019. *Freshwater export pathways from the Bay of Bengal*. Deep Sea Res. Pt. II 168, 104645.
https://doi.org/10.1016/j.dsr2.2019.104645

Isern-Fontanet, J., García-Ladona, E., Font, J., 2006. *Vortices of the Mediterranean Sea: An Altimetric Perspective*. J. Phys. Oceanogr. 36, 87–103.
https://doi.org/10.1175/JPO2826.1

Jensen, T., Wijesekera, H., Nyadjro, E., Thoppil, P., Shriver, J., Sandeep, K.K., Pant, V., 2016. *Modeling Salinity Exchanges Between the Equatorial Indian Ocean and the Bay of Bengal*. Oceanography 29, 92–101.
https://doi.org/10.5670/oceanog.2016.42

Ji, J., Ma, J., Dong, C., Chiang, J., Chen, D., 2020. *Regional Dependence of Atmospheric Responses to Oceanic Eddies in the North Pacific Ocean*. Remote Sens. 12, 1161.
https://doi.org/10.3390/rs12071161

Large, W.G., McWilliams, J.C., Doney, S.C., 1994. *Oceanic vertical mixing: A review and a model with a nonlocal boundary layer parameterization*. Rev. Geophys. 32, 363–403.
https://doi.org/10.1029/94RG01872

Lian, Z., Sun, B., Wei, Z., Wang, Y., Wang, X., 2019. *Comparison of Eight Detection Algorithms for the Quantification and Characterization of Mesoscale Eddies in the South China Sea*. J. Atmospheric Ocean. Technol. 36, 1361–1380.
https://doi.org/10.1175/JTECH-D-18-0201.1

Lin, P., Liu, H., Ma, J., Li, Y., 2019. *Ocean mesoscale structure–induced air–sea interaction in a high–resolution coupled model*. Atmospheric Ocean Sci. Lett. 12, 98–106.
https://doi.org/10.1080/16742834.2019.1569454

Marchesiello, P., McWilliams, J.C., Shchepetkin, A., 2003. *Equilibrium Structure and Dynamics of the California Current System*. J. Phys. Oceanogr. 33, 753–783.
https://doi.org/10.1175/1520-0485(2003)33<753:ESADOT>2.0.CO;2

Nigam, T., Pant, V., Prakash, K.R., 2018. *Impact of Indian ocean dipole on the coastal upwelling features off the southwest coast of India*. Ocean Dynam. 68, 663–676.
https://doi.org/10.1007/s10236-018-1152-x

Okubo, A., 1970. *Horizontal dispersion of floatable particles in the vicinity of velocity singularities such as convergences*. Deep Sea Res. Oceanogr. Abstr. 17, 445–454.
https://doi.org/10.1016/0011-7471(70)90059-8

Penven, P., Echevin, V., Pasapera, J., Colas, F., Tam, J., 2005. *Average circulation, seasonal cycle, and mesoscale dynamics of the Peru Current System: A modeling approach*. J. Geophys. Res. Oceans 110, 2005JC002945. https://doi.org/10.1029/2005JC002945

Rao, R.R., Girish Kumar, M.S., Ravichandran, M., Rao, A.R., Gopalakrishna, V.V., Thadathil, P., 2010. *Interannual variability of Kelvin wave propagation in the wave guides of the equatorial Indian Ocean, the coastal Bay of Bengal and the southeastern Arabian Sea during 1993–2006*. Deep Sea Res. Part Oceanogr. Res. Pap. 57, 1–13. https://doi.org/10.1016/j.dsr.2009.10.008

Sadhukhan, B., Chakraborty, A., 2023. *Role of local and remote forcing on the decadal variability of Mixed Layer Depth in the Bay of Bengal*. Dynam. Atmospheres Oceans 102, 101349. https://doi.org/10.1016/j.dynatmoce.2022.101349

Saji, N.H., Goswami, B.N., Vinayachandran, P.N., Yamagata, T., 1999. *A dipole mode in the tropical Indian Ocean*. Nature 401, 360–363. https://doi.org/10.1038/43854

Sandeep, K.K., Pant, V., 2018. *Evaluation of Interannual Simulations and Indian Ocean Dipole Events During 2000–2014 from a Basin Scale General Circulation Model*. Pure Appl. Geophys. 175, 4579–4603. https://doi.org/10.1007/s00024-018-1915-9

Shankar, D., Shetye, S.R., 1999. *Are interdecadal sea level changes along the Indian coast influenced by variability of monsoon rainfall?* J. Geophys. Res. Oceans 104, 26031–26042. https://doi.org/10.1029/1999JC900218

Shankar, D., Vinayachandran, P.N., Unnikrishnan, A.S., 2002. *The monsoon currents in the north Indian Ocean*. Prog. Oceanogr. 52, 63–120. https://doi.org/10.1016/S0079-6611(02)00024-1

Shchepetkin, A.F., McWilliams, J.C., 2005. *The regional oceanic modeling system (ROMS): a split–explicit, free–surface, topography–following-coordinate oceanic model*. Ocean Model. 9, 347–404. https://doi.org/10.1016/j.ocemod.2004.08.002

Shchepetkin, A.F., McWilliams, J.C., 2003. *A method for computing horizontal pressure–gradient force in an oceanic model with a nonaligned vertical coordinate*. J. Geophys. Res. Oceans 108, 2001JC001047. https://doi.org/10.1029/2001JC001047

Shchepetkin, A.F., McWilliams, J.C., 1998. *Quasi-Monotone Advection Schemes Based on Explicit Locally Adaptive Dissipation*. Mon. Weather Rev. 126, 1541–1580. https://doi.org/10.1175/1520-0493(1998)126<1541:QMASBO>2.0.CO;2

Sherin, C.K., Sarma, V.V.S.S., Rao, G.D., Viswanadham, R., Omand, M.M., Murty, V.S.N., 2018. *New to total primary production ratio (f-ratio) in the Bay of Bengal using isotopic composition of suspended particulate organic carbon and nitrogen*. Deep Sea Res. Oceanogr. Res. Pap. 139, 43–54. https://doi.org/10.1016/j.dsr.2018.06.002

Shetye, S.R., Gouveia, A.D., Shenoi, S.S.C., Sundar, D., Michael, G.S., Nampoothiri, G., 1993. *The western boundary current of the seasonal subtropical gyre in the Bay of Bengal*. J. Geophys. Res. Oceans 98, 945–954. https://doi.org/10.1029/92JC02070

Smagorinsky, J., 1963. *General circulation experiments with the primitive equations: I. The basic experiment*. Mon. Weather Rev. 91(3), 99–164. https://doi.org/10.1175/1520-0493(1963)091<0099:GCEWTP>2.3.CO;2

Song, Y., Haidvogel, D., 1994. *A Semi-implicit Ocean Circulation Model Using a Generalized Topography-Following Coordinate System*. J. Comput. Phys. 115, 228–244. https://doi.org/10.1006/jcph.1994.1189

Thompson, B., Gnanaseelan, C., Salvekar, P.S., 2006. *Variability in the Indian Ocean circulation and salinity and its impact on SST anomalies during dipole events*. J. Mar. Res. 64, 853–880. https://doi.org/10.1357/002224006779698350

Varna, M., Jithin, A.K., Francis, P.A., 2023. *Characteristics and dynamics of mesoscale eddies in the eastern Arabian Sea*. Deep Sea Res. Pt. II 207, 105218. https://doi.org/10.1016/j.dsr2.2022.105218

Weiss, J., 1991. *The dynamics of enstrophy transfer in two-dimensional hydrodynamics?* Phys. Nonlinear Phenom. 48, 273–294. https://doi.org/10.1016/0167-2789(91)90088-Q

Wunsch, C., 2020. *Is the Ocean Speeding Up?* Ocean Surface Energy Trends. J. Phys. Oceanogr. 50, 3205–3217. https://doi.org/10.1175/JPO-D-20-0082.1

Yadidya, B., Rao, A.D., 2022. *Interannual variability of internal tides in the Andaman Sea: an effect of Indian Ocean Dipole*. Sci. Rep. 12, 11104. https://doi.org/10.1038/s41598-022-15301-8

Yu, L., O'Brien, J.J., Yang, J., 1991. *On the remote forcing of the circulation in the Bay of Bengal*. J. Geophys. Res. Oceans 96, 20449–20454. https://doi.org/10.1029/91JC02424

Zeytounian, R., 1990. *The Boussinesq Approximation, in: Asymptotic Modeling of Atmospheric Flows*. Springer, Berlin, Heidelberg, 142–176. https://doi.org/10.1007/978-3-642-73800-5_8

Zhao, W.-W., Wang, J.-H., Wan, D.-C., 2020. *Vortex identification methods in marine hydrodynamics*. J. Hydrodynamics 32, 286–295. https://doi.org/10.1007/s42241-020-0022-4